



HAL
open science

The Effect of Heteroatom Doping on Nickel Cobalt Oxide Electrocatalysts for Oxygen Evolution and Reduction Reactions

Celia Belkessam, Selma Bencherif, Mourad Mechouet, Naima Idiri, Jalal Ghilane

► **To cite this version:**

Celia Belkessam, Selma Bencherif, Mourad Mechouet, Naima Idiri, Jalal Ghilane. The Effect of Heteroatom Doping on Nickel Cobalt Oxide Electrocatalysts for Oxygen Evolution and Reduction Reactions. *ChemPlusChem*, 2020, 85 (8), pp.1710-1718. 10.1002/cplu.202000436 . hal-02999632

HAL Id: hal-02999632

<https://hal.science/hal-02999632>

Submitted on 19 Nov 2020

HAL is a multi-disciplinary open access archive for the deposit and dissemination of scientific research documents, whether they are published or not. The documents may come from teaching and research institutions in France or abroad, or from public or private research centers.

L'archive ouverte pluridisciplinaire **HAL**, est destinée au dépôt et à la diffusion de documents scientifiques de niveau recherche, publiés ou non, émanant des établissements d'enseignement et de recherche français ou étrangers, des laboratoires publics ou privés.

Investigation of heteroatom's effect on nickel-cobalt oxide electrocatalyst for oxygen electrochemistry

Celia Belkessam¹, Selma Bencherif,^{2,3} Mourad Mechouet², Naima Idiri², Jalal Ghilane^{3*}

¹*Laboratoire de Traitement et Mise en Forme des Polymères de l'Université M'Hamed BOUGARA de Boumerdes, Algeria;*

²*Laboratoire de Physique et Chimie des Matériaux de l'Université Mouloud Mammeri de Tizi-Ouzou, Algeria;*

³*Université de Paris, ITODYS, UMR 7086 CNRS, SIELE Group, 15 rue J-A de Baïf, 75013, Paris, France*

Abstract

This work reports the synthesis of nickel cobalt oxides materials and their electrocatalytic performances toward the oxygen reduction and evolution reactions (ORR, OER). To this end, the nickel cobalt oxides have been synthesized using the sol-gel process with different precursors, nitrate, sulfate and chloride. All the samples are mesoporous and present similar diffraction patterns, indicating the formation of nickel cobalt oxides spinel structure with a nanoparticles size ranging from 35 to 65 nm. Besides this similarity, the physico-chemical properties differ depending on the nature of the selected precursor's including the materials morphology and the chemical composition. The catalytic activity toward ORR could be modulated between 2 and 4 electrons pathway depending on the used precursors. Thus, the sample generated with chloride exhibits the highest selectivity for the hydrogen peroxide production, within a large potential range (from -0.4 to 0.5V), while the sample generated from nitrate salts displays a preferential 2 plus 2 electrons. In addition, regarding the oxygen evolution reaction, the sample prepared using sulfate displays the highest performance. Overall, our results confirm that the precursor's chemical composition, used during the nanomaterials synthesis, leads to tune the electrocatalytic performances toward ORR and OER.

Keywords: Nickel cobalt oxide; Electrochemistry; Precursor's effect; Oxygen reduction reaction; Oxygen evolution reaction.

* Corresponding author.

E-mail addressee: jalal.ghilane@univ-paris-diderot.fr (J. Ghilane)

1. Introduction

For decades, the society has faced several crucial problems including the need for energy production and storage technologies [1]. Within this context, several researches focused on investigating viable alternatives and innovative solutions for green and sustainable chemistry establishment [2]. Electrochemical based technologies are one of the proposed options to reach those requirements [3]. Therefore, several reviews have been devoted to the development of electrochemical energy storage and conversion devices [4,5]. The oxygen electrochemistry, including the oxygen reduction reaction (ORR) and the oxygen evolution reaction (OER), are the most studied reactions in energy conversion systems such as fuel cells, metal-air batteries and for environmental issues especially for waste water treatment [6-8]. However, these reactions are very slow and involve multiple electrons transfer steps and requires significant activation energy. Thus, a catalyst must be used to attain higher efficiencies. The ORR process occurs through 4-electrons generating water, or 2-electrons reduction pathways with hydrogen peroxide as the main product [9,11]. The last process is less studied, even it allows to hydrogen peroxide production, which is one of the most important chemical products used in the industry, its production through the electrochemical ORR is less studied than the 4-electron pathway. Currently, platinum based materials and precious metal oxides (RuO_2 and IrO_2) are the state of the art catalyst displaying superior ORR and OER activity, respectively [12,13]. Besides these materials, several catalysts have been investigated including the non-precious metals and carbon based materials, leading to reach performances comparable to Pt based materials and IrO_2 [14,15]. The development of inexpensive (non-noble), more active and stable nanocatalysts is a crucial task to achieve excellent ORR and/or OER performances. In addition, these materials should have a high specific surface area to provide rich active sites, suitable porous structure for efficient mass transport and good conductivity [16].

Besides the classical electrocatalysts described above, transition metal oxides have attracted a wide attention due to their high stability, natural abundance, low cost, environmentally benign impacts and nontoxicity [17,19]. Different methods have been adopted to synthesis these materials, among them, the sol-gel chemistry, which is an attractive method since it has proven to be easy, low cost and successful soft approach frequently used to produce, at relatively low temperatures, a nanosized oxide powder, having usually a strong catalytic activity and relatively high stability [20]. Another advantage of the sol-gel route is the possibility to tune the precursor's solutions allowing the materials fabrication in a wide forms variety and properties, thus extending their

potential applications. Yuan *et al.* report that the used cobalt precursor's nature affects strongly the materials electrochemical and the catalytic performances towards ORR [21]. Shaikh *et al.* have studied the different precursor's effects on the electrochemical properties of manganese oxide thin films prepared by successive ionic layer adsorption [22].

Recently, mixed transition metal oxides (MTMO) received an increase interest due to their electrochemical and electrocatalytic properties, leading to their use in various applications, including supercapacitors, metal air batteries and fuel cells [23-26]. Within this materials class, spinel nickel cobaltite oxide ($\text{Ni}_x\text{Co}_{3-x}\text{O}_4$) has been reported as a promising materials [17,18]. Indeed, the generated materials provide several advantages including a high porosity and specific surface area. In addition, the presence of two transition metals (Ni and Co) provides to the composite with higher electrical conductivity and electrochemical activity. As an example the $\text{Ni}_{0.3}\text{Co}_{2.7}\text{O}_4$ supported on different materials has been investigated as electrocatalyst for OER and as electrode materials in supercapacitor devices [27,28]. However, a little attention has been devoted to this material electrochemical activity towards the ORR.

Herein, we report a systematic study on the used metallic precursors salts effects on the synthesized nickel cobalt oxide materials properties. As precursors, nickel and cobalt salts, charring the same anion nitrate, sulfate or chloride, were selected. The three synthesized nickel cobalt oxides were characterized by X-ray diffraction (XRD), scanning electron microscopy (SEM), Fourier Transformer Infra-Red spectroscopy (FTIR), X-ray photoelectron spectroscopy (XPS) and Brunauer-Emmett-Teller (BET). The surface analyses demonstrate the formation of spinel nickel cobalt oxides and that the Ni and Co oxidation states depend on the used precursor. In addition, the presence of metal chloride and metal sulfide on the annealed materials has been evidenced. Next, the electrocatalytic properties of the generated nickel cobalt oxides towards ORR and OER were evaluated. Our results demonstrate that the as-prepared nickel cobalt oxides exhibit a pronounced electrocatalytic activity towards ORR and OER. More interestingly, the material's electrocatalytic performances could be tuned depending on the used metallic salts anions.

2. Materials and method

2.1. Chemicals

The used precursors for the nanomaterials synthesis were, Ni(NO₃), Co(NO₃), Ni(SO₄), Co(SO₄), NiCl₂, CoCl₂ which are supplied from Merck. Citric acid was provided from Sigma-Aldrich. Potassium hydroxide (KOH from BiochemChemopharma) was used as supporting electrolyte for the electrochemical measurements.

2.2. Nickel cobalt oxides Synthesis

In this work, three different nickel cobalt oxides were synthesized using relatively similar procedure as reported in our previous work [29]. Briefly, 9 g of Co(SO₄) and 1 g of Ni(SO₄) were dissolved in 10 ml of distilled water and continuously stirred for 30 min. Next, a solution containing 14.85 g of citric acid, dissolved in 20 ml of distilled water, was added drop-wisely and a pink suspension solution was slowly formed. The mixture was then stirred for 2 h at room temperature before heating at 80 °C until a pink gel is formed. The latter was dried at 100 °C, for 3 h before being annealed for 2 h at 450 °C to obtain the final nickel cobalt oxide powder. Similar procedure was followed using the mixture Ni(NO₃)/Co(NO₃), and NiCl₂/CoCl₂, to obtain different samples labeled as Cl–NiCoO, N–NiCoO and S–NiCoO.

2.3. Material characterizations

X-ray diffraction (XRD) was used for the powders crystal phases identification and crystallites size estimation. The measurements were performed using a diffractometer (XPERT PRO, Cu K α radiation $\lambda=1.5418 \text{ \AA}$). The XRD profile was measured in 2θ range 10°–90° with a step width of 0.02° and collection time of 5 s. The generated materials specific surface area was estimated using the Brunauer–Emmett–Teller (BET) equation, after nitrogen adsorption measurement at 77.3 K, using a Quanta chrome NovaWin ©1994–2010, connected to Quanta chrome Instruments v11.0. Before the adsorption-desorption isotherm measurements, the samples were out gassed at 120 °C for 12 h. FTIR spectra were carried out using a Jasco 6300 spectrometer operating in ATR mode, with a wave number range of 4000–400 cm⁻¹. X-ray photoelectron spectroscopy (XPS) analysis were performed using a Thermo VG Scientific ESCALAB 250 system, fitted with a micro focused, monochromatic Al K α ($h\nu = 1486.6 \text{ eV}$). The nickel cobalt oxides morphologies and the microstructure were investigated using a Philips LS30 scanning electron microscope (SEM).

2.4. Electrochemical measurements

The electrocatalytic tests, of the synthesized nickel cobalt oxides generated with different precursors, were performed using a conventional three-electrode cell. A graphite rod and saturated calomel electrode (SCE) were used, as a counter and a reference electrode, respectively. The electrochemical measurements were performed in oxygen saturated aqueous electrolytic solution containing 0.1 mol L⁻¹ KOH. All the potentials have been converted to the reference hydrogen electrode (RHE). The electrochemical impedance spectroscopy (EIS) was performed in the frequency range 100000 to 1 Hz. The working electrode was a rotating ring disk electrode (RRDE) (E7R9 series®), from Pine Research Instruments and monitored by CHI920C bipotentiostat® (CH Instruments, Austin, Texas). The catalytic ink was prepared by dispersing under ultrasonication 1 mg of the nickel cobalt oxide with 380 µL of absolute ethanol, followed by the addition of 20 µL of Nafion® 117 solution (Sigma Aldrich). After that, 10 µL of the catalytic solution was drop casted onto the RRDE glassy carbon (GC) part with an estimated catalyst loading of 0.1 mg cm⁻². The catalysts electrochemical performances were evaluated using linear sweep voltammetry (LSV) at a scan rate 10 mV s⁻¹. The exchanged electrons number and the hydrogen peroxide production amount were evaluated using the following equations:

$$n_e = \frac{4I_D}{I_D + I_R / N} \quad \% H_2O_2 = \frac{200 * I_R / N}{I_D + I_R / N}$$

Where I_D is the faradic disk current and I_R is the corresponding faradic ring current and $N = 0.37$ is the collecting efficiency.

3. Results and discussion

3.1. Structural characterization

Thermogravimetric analyses (TGA) was first applied to investigate the thermal decomposition behavior on the dried nickel cobalt oxides powders generated using the tree different precursors (Figure 1a).

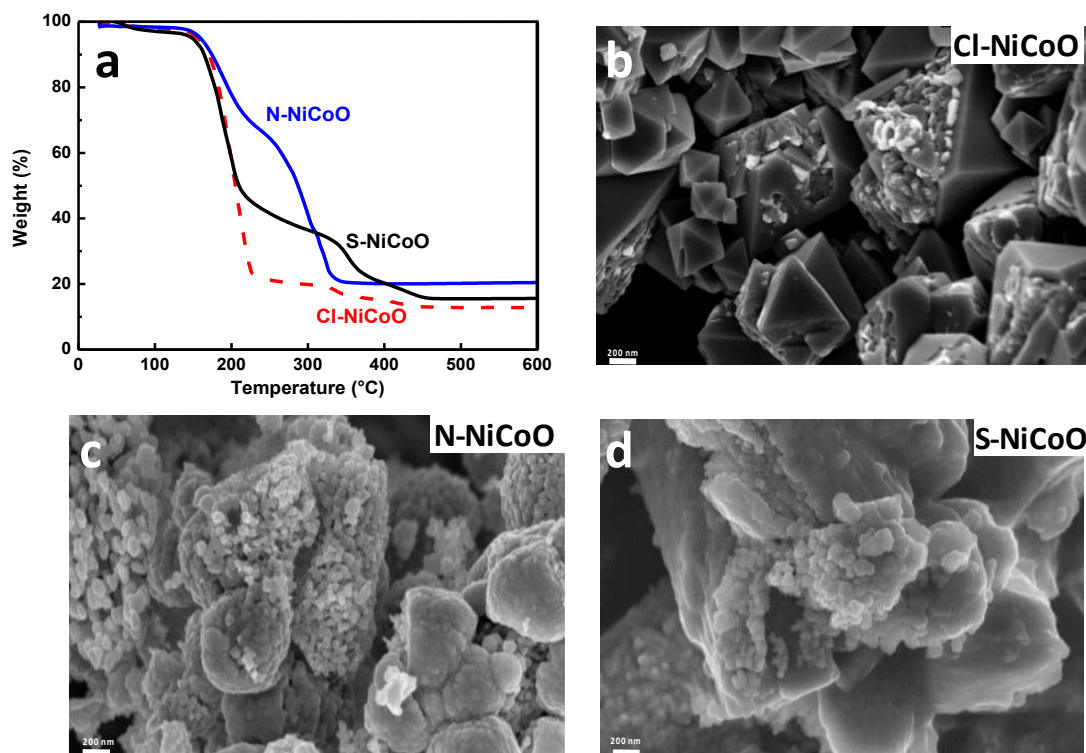


Figure 1 (a) TGA profiles of the dried nickel cobalt oxides powders (using different precursors) and before the annealing step. (b, c and d) SEM images of the generated nickel cobalt oxides using different precursors and after annealing at 450 °C.

For the three samples two major weight loss steps are observed at 230 and 350 °C. The first loss indicates the hydroxide precursor's decomposition, while the second weight loss corresponds to the inorganic precursor's decomposition and CO₂ removal [30,31]. For a temperature higher than 400 °C no significant weight loss was observed suggesting the precursor's total decomposition and the formation of the corresponding oxide phases. Based on the TGA results, the selected annealing temperature, in this work, was 450 °C for the three samples.

The synthesized nickel cobalt oxides morphologies are shown in Figure 1 b, c and d. The comparison of the SEM images clearly shows distinct structures depending on the precursor's nature. The oxide prepared using chloride salts exhibits homogenous pyramidal structured with angular faceted edges and a baseline diameter ranged from 200 to 400 nm. In the case of nitrate salts, globular structure was observed having of porous and interconnected particles. The particles have different sizes ranged from 20 to 200 nm. For S–NiCoO, the surface is inhomogeneous and full of visible agglomerates, with a random connective particles collection, having different geometries and sizes, were observed. Although the annealing process for the all samples was performed at the same temperature 450°C, the SEM investigations reveal that the nature of the anion's in the metallic salts

change drastically the generated materials morphology. Besides that, the SEM images suggest the presence of different porosity depending on the used precursor. Similarly, morphological changes have been reported for the manganese oxide prepared by acetate, chloride and sulfate precursors [22].

Next, the generated materials were further characterized using XRD and BET methods. Figure 2a presents the X-ray diffraction (XRD) patterns of the nickel cobalt oxides obtained from various precursors.

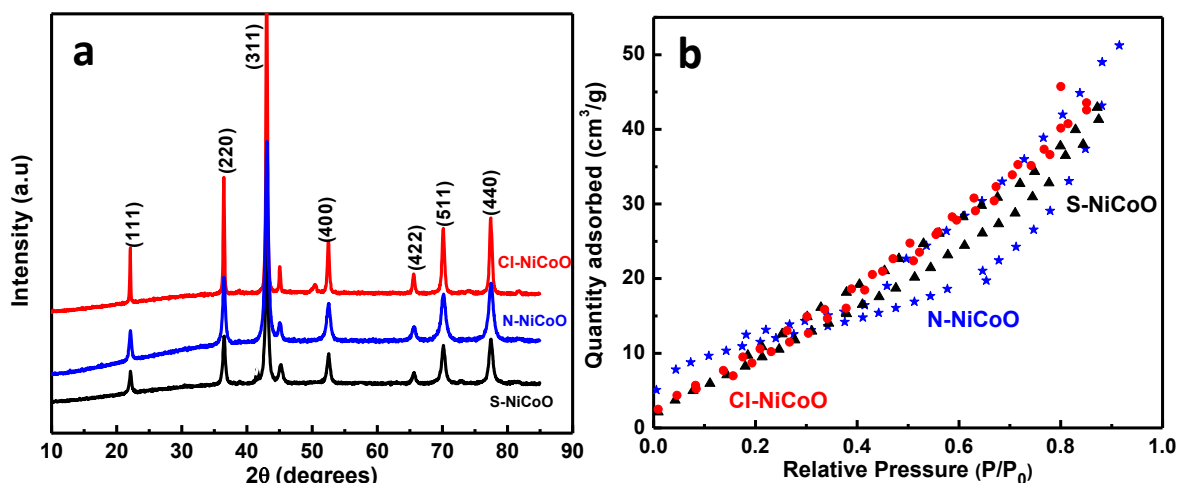


Figure 2 (a) XRD patterns of the three generated nickel cobalt oxides. (b) Nitrogen adsorption/desorption isotherms.

All the samples display the same diffraction lines with four apparent characteristic peaks observed at 2θ about 22, 36.4, 42.8, which could be assigned to (111), (220), (311), and (400) plane, in a good agreement with the literature (JCPDS card no 73-1702) [29,32,33]. Compared to the others published works, a small peaks shift to lower angles was observed suggesting change in the lattice parameters. The sample prepared using Cl precursor displays an additional weak diffraction peak at 50.5° indicating the co-existence of a small amount of CoO (PDF 43-1004) [21]. The XRD analysis indicates that the as-prepared material crystalline structure was not altered by varying the precursor's nature. However, the peaks sharpness changes as well as the intensity, suggesting the growth in the oxide's crystallites size from 35, 52 to 65 nm for N-NiCoO, S-NiCoO and Cl-NiCoO, respectively. The observed patterns confirm that the obtained nickel cobalt oxides have a spinel structure [34,35]. In this configuration, the nickel ions are positioned only at the octahedral sites, while the cobalt ions are dispersed over the octahedral and the tetrahedral sites and the oxygen atoms are situated in the faces [36,37].

The structural characterization was complemented by the BET analysis. For all the samples, the adsorption/desorption isotherms, shown in Figure 2b, display the classic shape type IV isotherm shape and H1-type hysteresis [38]. The N₂ uptake, for all the samples, starts at a relative pressure around 0.4 followed by a gradual increase, suggesting the presence of small pores size [30]. These oxides exhibit a high surface area with mesoporous nano-powders. The BET data and the corresponding pores size distribution curve, derived from the adsorption branch by the Barrett–Joyner–Halenda (BJH) method, For the three samples, similar pore size distribution is observed around 2 nm, which is ideal pore size dimension for ions and electrons diffusion within the materials [39]. Besides that, the highest measured BET surface area was found to be 56 m².g⁻¹ for the Cl–NiCoO while a value of 49 and 41 m².g⁻¹ was observed for S–NiCoO and N–NiCoO, respectively. This tendency was also confirmed by the measured BJH surface area. The BET surface area values are similar to those reported in the literature for nickel cobalt oxides material's annealed at temperature ranged from 400 to 550°C [28,40].

3.2. Surface characterization

The chemical and elemental compositions of the generated materials were investigated by FTIR and XPS spectroscopy. Figure 3 displays the FTIR spectra of the nickel cobalt oxides powders prepared from various precursors, after being annealed at 450°C.

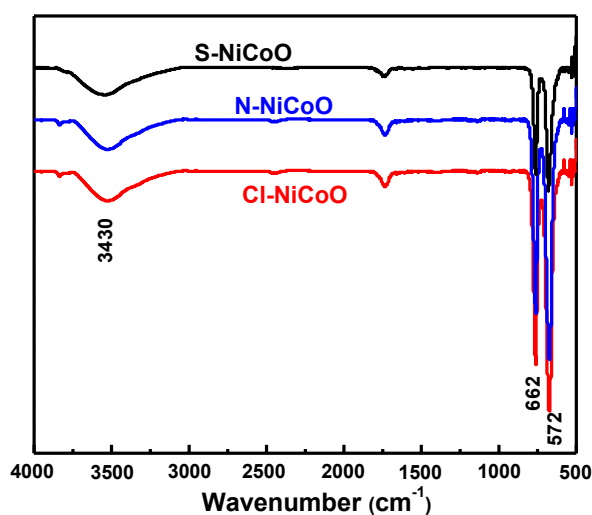


Figure 3 Annealed nickel cobalt oxides FTIR spectra

The three investigated samples display the same FTIR spectra with two intense peaks located at 572, 662 cm⁻¹ and two broad peaks at 1626 and 3430 cm⁻¹, which are a characteristic of the nickel cobalt oxide spinel structure formation [29]. These peaks at lower frequencies are assigned to the metal oxygen bond stretching vibrations of the Ni–O

and Co—O, respectively [41]. They correspond to the metal ion that occupies the tetrahedral and octahedral sites in the spinel structure [42,43]. The broad peak at around 3430 cm^{-1} and the peak at 1626 cm^{-1} are attributed to the hydroxyl groups stretching and bending modes of physically absorbed water molecules [44]. For all the samples, the absence of absorption peak in the range $1000\text{--}1500\text{ cm}^{-1}$ and $1800\text{--}2500\text{ cm}^{-1}$, indicates the absence of carbon sources (C=O and C=H stretching-mode). This result suggests the organic part complete decomposition within the precursors at the selected annealing temperature (450°C).

X-ray photoelectron spectroscopy (XPS) measurements were performed to investigate the surface compositions and chemical states of the generated nickel cobalt oxides. The corresponding results were presented in Figure 4.

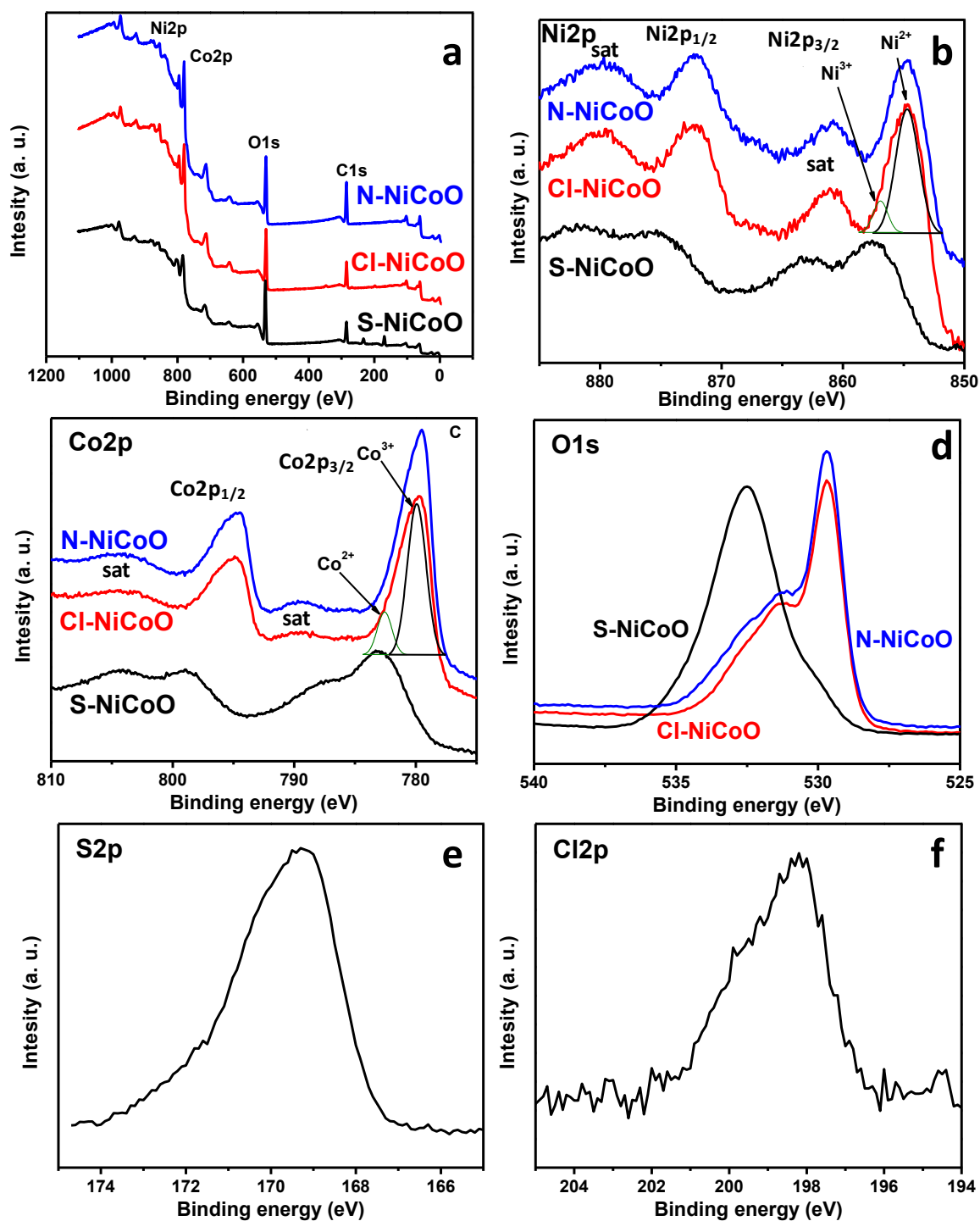


Figure 4 (a) Survey XPS spectra of the three annealed nickel cobalt oxides (b) high XPS resolution spectra of Ni 2p, (c) Co 2p, (d) O 1s, (e and f) high XPS resolution spectra of S 2p and Cl 2p in S–NiCoO and Cl–NiCoO, respectively.

As shown in the XPS survey spectrum (Figure 4a), the signals of the elements Ni 2p, Co 2p and O 1s can be observed, demonstrating the existence of nickel, oxygen, and cobalt elements in the sample. The C1s signal is mainly due to the surface contamination. In addition, deep analysis of the XPS survey confirms the presence of C1s at the extreme

surface (substrate contamination), as attested by the lack of background change before and after the C1s signal. However, for the other elements O 1s, Co 2p and Ni 2p the background increases, after the corresponding peaks, due to the photoelectrons inelastic scattering suggesting the presence of those elements inside the material [45]. The core level spectrum of Ni2p was reported in Figure 4b and shows two different behaviors. The Ni2p spectra of the samples N–NiCoO and Cl–NiCoO display a peak at 854.6 eV corresponding to Ni2p_{3/2} and a peak at 872 eV for Ni2p_{1/2}, both peaks are followed by a satellite [46]. These peaks are assigned to the Ni²⁺ oxidation state. The Ni2p spectra could be deconvoluted using two fitted peaks, with a major contribution from Ni²⁺ and a minor contribution from Ni³⁺ at 857 eV [47,48]. However, for the S–NiCoO sample, the main peak of Ni is located at 857 and 875 eV for Ni2p_{3/2} and Ni2p_{1/2}, respectively. Contrarily to the other samples, the predominant oxidation state is Ni³⁺ and a small contribution of Ni²⁺ is observed at 854.6 eV. Figure 4c shows the XPS Co2p high resolution spectra, for the three samples, with two major peaks and two satellites. Similarly to Ni2p, the samples N–NiCoO and Cl–NiCoO display the same shape and peaks position. Thus, the first peak is observed at a binding energy of 779.6 eV and the second is located at 794.5 eV [49]. The peak of Co2p_{3/2} could be deconvoluted using two fitted peaks, with Co³⁺ as a major oxidation state (at 779.6 eV) and a Co²⁺ small contribution at 782 eV. However, for the S–NiCoO sample, the predominant peak is located at 782 eV assigned to Co²⁺ associated to a small contribution of Co³⁺ [50,51]. Overall, for the samples N–NiCoO and Cl–NiCoO, the predominant oxidation state within the nickel cobalt oxides material are Ni²⁺ and Co³⁺, while for the S–NiCoO sample the Ni³⁺ and Co²⁺ are the main oxidation states. Besides, the O1s spectra for the N–NiCoO and Cl–NiCoO (Figure 4d) exhibit a major peak at 529.6 eV and two shoulders at higher binding energy 531.3 and 532.5 eV. The peak observed at 529.6 eV corresponds to the metal oxygen bond (M–O) and the shoulder observed at 531.3 eV is attributed to the defect sites with a lowest oxygen coordination, while the oxygen at 532.5 eV is a signature of chemical and/or physical surface bonded water [39,52]. Contrarily, the S–NiCo sample exhibits a main peak at 532.5 eV and a shoulder at lower energy of 529.6 eV. In addition to the major components, Cl, S and N elements were detected on the sample Cl–NiCoO, S–NiCoO and N–NiCoO, respectively. The S2p spectrum could be deconvoluted using two contributions at binding energy 168.2 and 170.5 eV confirming the presence of S–O bond in the sulfate form. In addition, the absence of peak at lower binding energy in the region from 161 to 164 eV suggests the absence of M–S bond. However, the peak of Cl2p is observed at binding

energy lower than 200 eV indications the presence of metal chloride bond. These results indicate that the Cl, S and N could be considered as a doping element of the synthesized nickel cobalt oxides materials. The nickel cobalt oxide spinel structure has a general formula $\text{Ni}_x\text{Co}_{3-x}\text{O}_4$. In the case of Cl–NiCoO and N–NiCoO, the XPS results reveal that the major oxidation states are Ni^{2+} and Co^{3+} suggesting a x value higher than 0.6. While for S–NiCoO the main oxidation states are Ni^{3+} and Co^{2+} suggestion a x value bellow 0.6 as well as the presence of sulfate [33].

3.3. Electrochemical oxygen reduction and evolution studies

The generated materials electrocatalytic activities toward the ORR were investigated. The LSV curves, on the RRDE disk electrode, were performed in O_2 -saturated KOH (0.1 mol L^{-1}) solution at 1600 rpm by scanning potential from 1 V to -0.4 V at 10 mV s^{-1} scan rate (Figure 5a).

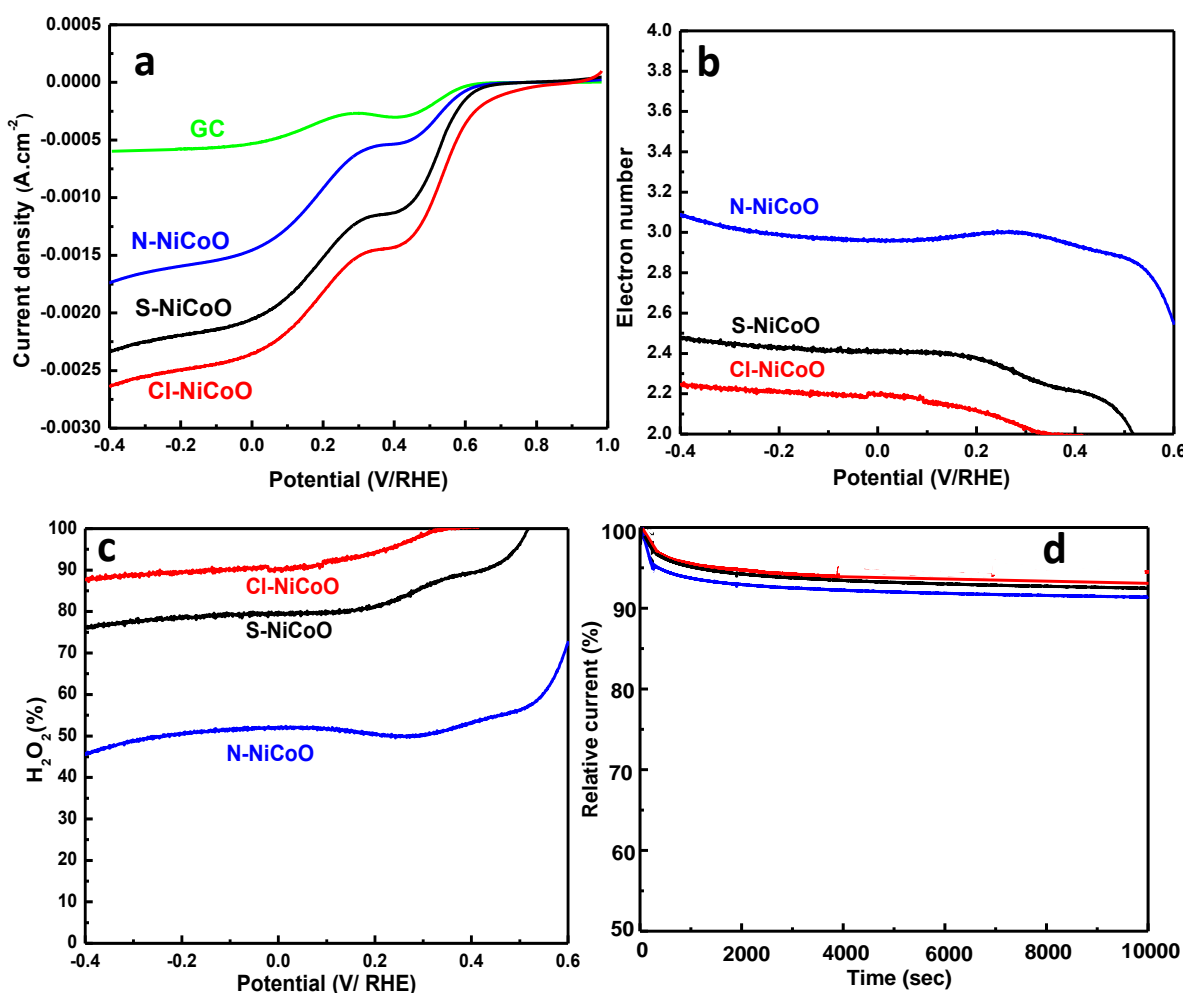


Figure 5 ORR performances of the three nickel cobalt oxides samples Cl–NiCoO, N–NiCoO and S–NiCoO (a) LSV curves in O_2 -saturated 0.1 mol L^{-1} KOH solution at 1600 rpm and 10 mV s^{-1} as a scan rate. (b) The electron number variation as function of the potential. (c) The variation of the hydrogen peroxide percentage versus the potential. (d)

Variation of the relative current versus time in 0.1 mol L⁻¹ KOH at an applied potential of 0.2 V/RHE.

Compared to the bare glassy carbon electrode and whatever the used precursor, the LSV's curves show clearly that the nickel cobalt oxides electrodes exhibit pronounced ORR electrocatalytic activity. For all investigated materials, the curves exhibit two reduction waves suggesting the presence of two consecutive electrons reduction steps, with the production of hydrogen peroxides during the first reduction. The LSV's comparison reveals that the onset (E_{onset}) and half-wave ($E_{1/2}$) potentials of the nickel cobalt oxides electrodes change depending on the used precursor. The electrocatalyst N–NiCoO displays the lowest performance with an onset potential at 0.6 V/RHE and a limiting diffusion current density at $-1.7 \text{ mA}\cdot\text{cm}^{-2}$. The S–NiCoO shows an onset potential at 0.63 V and a maximum current density around $-2.3 \text{ mA}\cdot\text{cm}^{-2}$. The sample Cl–NiCoO, shows the best performance as attested by the positive shift of the onset value measured at 0.7 V/RHE and a highest limiting current density ($-2.5 \text{ mA}\cdot\text{cm}^{-2}$).

In order to get more insight about the different performances towards ORR, the transferred electrons numbers, as well as the hydrogen peroxide production amount (% H_2O_2) were calculated as shown in Figure 5.b and c, respectively. The results reveal that the two previous parameters depend strongly on the used precursor's nature. Within a large potential range from -0.4 to 0.6 V, the ORR catalyzed by Cl–NiCoO proceeds preferentially through two-electrons-transfer reaction with a measured value around 2.2. For the H_2O_2 production, the efficiency is as high as 90% in the potential region from 0.2 to -0.2 V, and decreases slightly for lower potential reaching a value of 86% at -0.4 V. For the sample S–NiCoO the electrons transfer number is around 2.4 and the H_2O_2 percentage is varied between 70 to 80%, for a potential range from 0.2 to -0.4 V. However, the N–NiCoO displays an electrons transfer number around 3 and the H_2O_2 percentage is below 50%. The electrochemical impedance spectroscopy (EIS) investigation shows that the charge transfer resistance of Cl–NiCoO is 120 Ω , which is slightly smaller than those of S–NiCoO (134 Ω) and N–NiCoO (168 Ω). All these results suggest that the Cl–NiCoO is an efficient electrocatalyst for the electrochemical oxygen reduction, through 2 electrons pathway, with high selective production of H_2O_2 . In addition, the precursor change leads to modulate the electrochemical reduction of oxygen from a preferential 2 electrons to a mixed 2 plus 2 electrons. Seemingly, the difference in the catalytic properties could be related to the change in the morphology as well as the presence of precursor anion which

could act as doping element and thus affect the distribution of the active site [53]. The Cl–NiCoO shows a pyramidal structure with angular faceted edges and has the highest surface area, which may facilitate the oxygen diffusion to the electrocatalytic active sites. In addition, the presence of metal-chloride (as confirmed by XPS) could induce several effects, including an efficient oxygen adsorption and the intermediates species release through the electrostatic interactions and through the efficient O–O bond activation/cleavage. Furthermore, the presence of chloride anion at the extreme surface could participate in the oxygen solubility enhancement, thus, favors the oxygen adsorption and participate in the release of intermediates species through the electrostatic interactions [54]. The stability of the different nickel cobalt oxides electrodes was tested by recording the relative current variation as a function of time at a constant potential of 0.2 V during 10000 s (figure 5d). All the tested materials display a large stability with a relative current up to 92% for a period up to 10000 s. During the first 1000 s, a slight decrease in the relative current is observed and then stabilizes at 95%, for a long period up to 10000 s. The Cl–NiCoO electrode was found to be slightly more stable than the two other electrodes. Besides the ORR, the OER is the reverse reaction which, has been extensively studied for water splitting and metal-air batteries [55,56]. In the literature, several works describe the bi-functional catalysts with an efficient catalytic activity toward the ORR and OER [57,58]. The as-prepared nickel cobalt oxides electrocatalytic activity towards OER was evaluated in alkaline solution. Figure 6 compare the OER linear sweep voltammetry curves of the three nickel cobalt oxides samples.

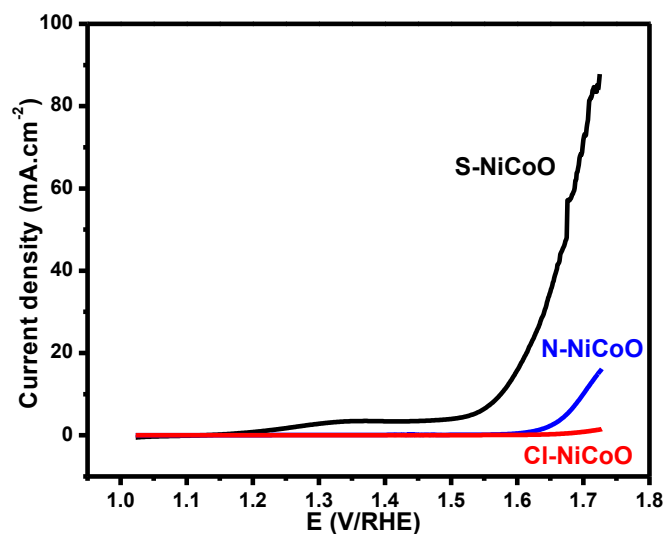


Figure 6 OER of the three nickel cobalt oxides samples Cl–NiCoO, N–NiCoO and S–NiCoO. LSV curves recorded on the three nickel cobalt oxides sample in 0.1 mol L⁻¹ KOH solution at a scan rate 10 mV.s⁻¹.

The LSV's curves comparison shows the presence of catalytic activity towards the OER, for the samples N–NiCoO and S–NiCoO, while the Cl–NiCoO sample shows the lowest performance. Interestingly, the S–NiCoO displays the highest catalytic activity towards the OER, as attested by a lowest onset potential and a highest current density. The S–NiCoO LSV curve shows a small oxidation peak at 1.35 V, corresponding to the formation of Ni³⁺ or Ni⁴⁺ species [59]. As the XPS investigations demonstrate that in the S–NiCoO sample the predominant oxidation states is Ni³⁺, the observed oxidation peak would be attributed to Ni⁴⁺, which is known to be an active catalytic site for the OER [60]. The other important parameter for the OER is the over-potential value at current density of 10 mA.cm⁻². This metric value is reached for an over-potential value of 0.340 V, which is comparable to the best performance of other nickel cobalt oxides reported in the literature [33,40,61]. Recently, heteroatoms (S, N, P) doped transition metal have been reported to be an efficient approach for enhancing the catalytic activities [62,63]. The pronounced OER performance is linked to the main Ni³⁺ oxidation state of Ni on S–NiCoO and also to the presence of sulfide which increase the number of active sites, change the chemical as well as the coordination of Ni/Co [64].

4. Conclusions

In summary, several nickel cobalt oxides were prepared using three different metallic salts with nitrate, sulfite and chloride as anions. The generated materials were annealed at the same temperature 450 °C. Next, the different materials characterizations confirm the formation of nickel cobalt oxides spinel structure and similar XRD patterns were obtained. However, change in the morphology and the physicochemical properties, including the surface area and the pore size were observed, depending on the used precursor. In addition, the XPS investigations reveal that the Ni and Co oxidation states were found to be depending on the used precursors. Interestingly, the sulfate anion, used as precursor, shows a predominant Ni³⁺ and Co²⁺, while the others anions present Ni²⁺ and Co³⁺, as the main oxidation states. Next, the as-prepared nickel cobalt oxides catalytic performance towards the ORR and OER were investigated. As a result, the nanomaterials display a preferential oxygen reduction through a 2 electrons pathway in the following order Cl–NiCoO, S–NiCoO and N–NiCoO. However, for the OER, the S–NiCoO sample displays the highest electrocatalytic performance. Overall, this work demonstrates that changing the precursor's nature makes possible to tune the nickel cobalt oxide catalyst electrochemical performance. We anticipate that this strategy could be extended to others mixed transition

metal oxides and could lead to the development of an efficient electrocatalyst but also for a bi-functional electrocatalyst.

Acknowledgments

The authors thank Dr. Philippe Decorse for performing the XPS measurements. Special thanks to Mr Taher MERZOUK for BET analyses. C. Belkessam thanks the University of M'Hamed BOUGARA de Boumerdes, Algeria for the financial support of the exchange student program. S. Bencherif thanks the program Profas B+ and Campus France for the financial support.

References

-
- [1] Z.L. Wang, D. Xu, J.J. Xu, X.B. Zhang, *Chem. Soc. Rev.* 43 (2014) 7746–7786.
 - [2] X. Zou, Y. Zhang, *Chem. Soc. Rev.* 44 (2015) 5148–5180.
 - [3] P.G. Bruce, S.A. Freunberger, L.J. Hardwick, J.M. Tarascon, *Nat. Mater.* 11 (2012) 19–29.
 - [4] M. Shao, Q. Chang, J.P. Dodelet, R. Chenitz, *Chem. Rev.* 116 (2016) 3594–3657.
 - [5] N.T. Suen, S.F. Hung, Q. Quan, N. Zhang, Y.J. Xu, H.M. Chen, *Chem. Soc. Rev.* 46 (2017) 337–365.
 - [6] Y. Bu, O. Gwon, G. Nam, H. Jang, S. Kim, Q. Zhong, J. Cho, G. Kim, *ACS Nano* 11 (2017) 11594–11601.
 - [7] J. Wang, Y. Gao, D. Chen, J. Liu, Z. Zhang, Z. Shao, F. Ciucci, *ACS Catal.* 8 (2018) 364–371.
 - [8] J. Yu, Y. Zhong, X. Wu, J. Sunarso, M. Ni, W. Zhou, Z. Shao, *Adv. Sci.* 5 (2018) 1800514.
 - [9] Y. Nie, L. Li, Z. Wei, *Chem. Soc. Rev.* 44 (2015) 2168–2201
 - [10] J.M. Campos-Martin, G. Blanco-Brieva, J.L.G. Fierro, *Angew. Chem. Int. Ed.* 45 (2006) 6962–6984.
 - [11] Y. Kofuji, S. Ohkita, Y. Shiraishi, H. Sakamoto, S. Tanaka, S. Ichikawa, T. Hirai, *ACS Catal.* 6 (2016) 7021–7029.
 - [12] D. Wang, H.L. Xin, R. Hovden, H. Wang, Y. Yu, D.A. Muller, F.J. DiSalvo, H.D. Abruña, *Nat. Mater.* 12 (2013) 81–87.
 - [13] T. Reier, M. Oezaslan, P. Strasser, *ACS Catal.* 2 (2012) 1765–1772.
 - [14] W.T. Hong, M. Risch, K.A. Stoerzinger, A. Grimaud, J. Suntivich, Y. Shao-Horn, *Energy Environ. Sci.* 8 (2015) 1404–1427.
 - [15] R. Borup, J. Meyers, B. Pivovar, Y.S. Kim, R. Mukundan, N. Garland, D. Myers, M. Wilson, F. Garzon, D. Wood, P. Zelenay, K. More, K. Stroh, T. Zawodzinski, J. Boncella, J.E. McGrath, M. Inaba, K. Miyatake, M. Hori, K. Ota, Z. Ogumi, S. Miyata, A. Nishikata, Z. Siroma, Y. Uchimoto, K. Yasuda, K. Kimijima, N. Iwashita, *Chem. Rev.* 107 (2007) 3904–3951.
 - [16] E. Rios, S. Abarca, P. Daccarett, H. Nguyen Cong, D. Martel, J.F. Marco, J.R. Gancedo, J.L. Gautier, *Int. J. Hydrogen Energy* 33 (2008) 4945–4954.
 - [17] A.K. Yedluri, H.J. Kim, *RSC Adv.* 9 (2019) 1115–1122.
 - [18] N.T. Suen, S.F. Hung, Q. Quan, N. Zhang, Y.J. Xu, H.M. Chen, *Chem. Soc. Rev.* 46 (2017) 337–365.
 - [19] L. Han, S. Dong, E. Wang, *Adv. Mater.* 28 (2016) 9266–9291.

-
- [20] M. Fu, Y. Li, S. Wu, P. Lu, J. Liu, F. Appl. Surf. Sci. 258 (2011) 1587–1591.
- [21] X. Yuan, X.X. Hu, X.L. Ding, H.C. Kong, H.D. Sha, H. Lin, W. Wen, G. Shen, Z. Guo, Z.F. Ma, Y. Yang, Nanoscale Res. Lett. 8 (2013) 478–489.
- [22] A.A. Shaikh, M.R. Waikar, R.G. Sonkawade, Synth. Met. 247 (2019) 1–9.
- [23] F. Cheng, J. Shen, B. Peng, Y. Pan, Z. Tao, J. Chen, Nat. Chem. 3 (2011) 79–84.
- [24] G. Gupta, K. Selvakumar, N. Lakshminarasimhan, S.M.S Kumar, M. Mamlouk, J. Power Sources 461 (2020) 228131
- [25] L. Zhou, D. Zhao, X.W. Lou, Adv. Mater. 24 (2012) 745–748.
- [26] J.S. Hong, H. Seo, Y.H. Lee, K.H. Cho, C. Ko, S. Park, K.T. Nam, *Small Methods* 4 (2020) 3.
- [27] F. Lu, M. Zhou, Y. Zhou, X. Zeng, Small 13 (2017) 1701931.
- [28] H.B. Wu, H. Pang, X.W.D. Lou, Energy Environ. Sci. 6 (2013) 3619–3626.
- [29] C. Belkessam, M. Mechouet, N. Idiri, A. Kadri, N. Djelali, Mater. Res. Express 6 (2019) 105032.
- [30] G. Rajeshkhanna, E. Umeshbabu, P. Justin, G.R. Rao, Int. J. Hydrogen Energy 40 (2015) 12303–12314.
- [31] D.P. Dubal, P. Gomez-Romero, B.R. Sankapal, R. Holze, Nano Energy 11 (2015) 377–399.
- [32] N. Padmanathan, S. Selladurai, RSC adv. 4 (2014) 8341–8349.
- [33] M. Cui, X. Ding, X. Huang, Z. Shen, T.L. Lee, F.E. Oropeza, J.P. Hofmann, E.J.M. Hensen, K.H.L. Zhang, Chem. Mater. 31 (2019) 7618–7625.
- [34] M. Lenglet, R. Guillaumet, J. Dürr, D. Gryffroy, R.E. Vandenberghe, Solid State Commun. 74 (1990) 1035e9.
- [35] J. Du, G. Zhou, H. Zheng, C. Cheng, J. Ma, W. Wei, L. Chen, T. Wang, ACS Appl. Mater. Interfaces 5 (2013) 7405–7409.
- [36] H.W. Wang, Z.A. Hu, Y.Q. Chang, Y.L. Chen, H.Y. Wu, Z.Y. Zhanga, Y.Y. Yanga, J. Mater. Chem. 21 (2011) 10504–10511.
- [37] L. Shen, Q. Che, S. Li, X. Zhang, Adv. Funct. Mater. 24 (2014) 2630–2637.
- [38] F.H. Rouquerol, J. Rouquerol, K. Sing, Adsorption by powders and porous solids. London: Academic Press; 1999.
- [39] P. Syedvali, G. Rajeshkhanna, E. Umeshbabu, G.U. Kiran, G.R. Rao, P. Justin, RSC Adv. 5 (2015) 38407–38416.
- [40] J. Zho, Y. He, Z. Chen, X. Zheng, X. Han, D. Rao, C. Zhong, W. Hu, Y. Deng, ACS Appl. Mater. Interfaces 11 (2019) 4915–4921.
- [41] E. Umeshbabu, G. Rajeshkhanna, G.R. Rao, Int. J. Hydrogen energy 39 (2014) 15627–15638.
- [42] H. Guan, C. Shao, Y. Liu, N. Yu, X. Yang, Solid State Commun. 131 (2004) 107–109.
- [43] W. Luo, H. Xianluo, Y. Sun, Y.J. Huang, Mater Mater. Chem. 22 (2012) 8916–8921.
- [44] D.C. Marcano, D.V. Kosynkin, J.M. Berlin, A. Sinitskii, Z. Sun, A. Slesarev, L.B. Alemany, W. Lu, J.M. Tour, ACS Nano. 4 (2010) 4806–4814.
- [45] S. Bouden, A. Dahi, F. Hauquier, H. Randriamahazaka, J. Ghilane, Scientific Reports 6 (2016) 36708.
- [46] X. Yu, Z. Sun, Z. Yan, B. Xiang, X. Liu, P. Du, J. Mater. Chem. A 2 (2014) 20823–20831.
- [47] J. Tian, J. Chen, J. Liu, Q. Tian, P. Chen, Nano Energy 48 (2018) 284–291.
- [48] Y. Zhang, H. Wang, B. Liu, X. Zhao, Y. Wei, Appl. Surf. Sci. 504 (2020) 144598.
- [49] Y. Zhang, B. Wang, F. Liu, J. Cheng, X.W. Zhang, L. Zhang, Nano Energy 27 (2016) 627–637.

-
- [50] S. Wang, M. Chen, Y. Xie, Y. Fan, D. Wang, J.-J. Jiang, Y. Li, H. Grutzmacher, C.Y. Su, *Small* 12 (2016) 2365-2375.
- [51] H. Geng, Y. Guo, X. Ding, H. Wang, Y. Zhang, X. Wu, J. Jiang, J. Zheng, Y. Yang, H. Gu, *Nanoscale* 8 (2016) 7688-7694.
- [52] C. Guan, X. Liu, W. Ren, X. Li, C. Cheng, J. Wang, *Adv. Energy Mater.* 7 (2017) 1602391.
- [53] K. Imran, K. Ramya, P.C. Ghosh, A. Sarkar, N. Rajalakshmi, *ACS Appl. Energy Mater.* 2 (2019) 7811–7822.
- [54] T. N. Pham-Truong, T. Petenzi, C. Ranjan, H. Randriamahazaka, J. Ghilane, *Carbon* 130 (2018) 544–552.
- [55] Y. Li, S. Chen, D. Xi, Y. Bo, R. Long, C. Wang, L. Song, Y. Xiong, *Small* 14 (2018) 1702109.
- [56] A. Seong, J. Kim, O. Kwon, H.Y. Jeong, R.J. Gorte, J.M. Vohs, G. Kim, *Nano Energy* 71 (2020) 104564.
- [57] T. N. Pham-Truong, H. Randriamahazaka, J. Ghilane, *ACS Catal.* 8 (2018) 869–875.
- [58] J. Zhang, Z. Zhao, Z. Xia, L. Dai, *Nat. Nanotech.* 10 (2015) 444–452.
- [59] X. Lu, C. Zhao, *Nat. Comm.* 6 (2015) 6616–6623.
- [60] M.W. Louie, A.T. Bell, *J. Am. Chem. Soc.* 135 (2013) 12329–12337.
- [61] C. Zhu, D. Wen, S. Leubner, M. Oschatz, W. Liu, M. Holzschuh, F. Simon, S. Kaskel, A. Eychmüller, *Chem. Commun.* 51 (2015) 7851–7854.
- [62] S. Lalwani, A. Joshi, G. Singh, R.K. Sharma, *Electrochimica Acta* 328 (2019) 135076.
- [63] M.A.R. Anjum, M.D. Bhatt, M.H. Lee, J.S. Lee, *Chem. Mater.* 30 (2018) 8861–8870.
- [64] M. Gao, L. He, Z.Y. Guo, Y.R. Yuan, W.W. Li, *ACS Appl. Mater. Interfaces* 12 (2020) 443–450.

